Available online at www.sciencedirect.com
SCIENCE DIRECT®
Journal of Magnetic Resonance 171 (2004) 80–89
JMR Journal of Magnetic Resonance
www.elsevier.com/locate/jmr

Absorption line CW EPR using an amplitude modulated longitudinal field

Matvey Fedin*,[1], Igor Gromov[2], Arthur Schweiger*

Physical Chemistry Laboratory, Department of Chemistry and Applied Biosciences, ETH-Hönggerberg, 8093 Zürich, Switzerland

Received 25 June 2004; revised 27 July 2004
Available online 9 September 2004

Abstract

In standard continuous wave electron paramagnetic resonance (CW-EPR) experiments, the first derivative of absorption lines is detected. This type of a line shape is caused by the magnetic field modulation and is usually an undesired feature, since the sensitivity of CW-EPR drastically decreases with increasing linewidth. A new approach is introduced, which allows for the measurement of absorption line EPR spectra in systems with broad inhomogeneous lines. The method makes use of multiple-photon transitions that are induced in spin systems when a transverse microwave and a longitudinal radio frequency field are simultaneously applied. The absorption lines are obtained by using amplitude modulation of the radio frequency field and slight saturation of the spectral lines. The basics of the new approach are discussed and experimental examples are given.

Keywords: Electron paramagnetic resonance; EPR; ESR; Modulation; Absorption line shapes; Multiple photon transitions

1. Introduction

In electron paramagnetic resonance (EPR), modulation of the magnetic field followed by phase-sensitive detection is routinely used to increase the sensitivity of continuous wave (CW) EPR experiments [1]. As a result of the field modulation, derivative-like line shapes rather than absorption lines are recorded. A quantum-mechanical interpretation of CW-EPR proposed recently, provides for a deeper insight into the physical process behind this experiment [2]. It was shown, that the EPR lines are formed by multiple-photon transitions induced by a transverse microwave (mw) and a longitudinal radio frequency (rf) field.

The detection of EPR spectra with derivative-like line shapes has several disadvantages. The major disadvantage is that sensitivity drops rapidly for samples with broad EPR lines [1]. This is because the EPR signal intensity changes only slightly as a function of the magnetic field, so that field modulation does not significantly alter the detected signal. Thus large modulation amplitudes have to be used, which may cause distortions of the baseline and are usually limited to about 4 mT. A minor disadvantage is the more complex interpretation of the spectra and their comparison to absorption spectra obtained with other techniques. In principle, this can be remedied by integrating the spectrum, which is expected to result in the pure absorption spectrum. However, for weak signals the obtained absorption spectrum suffers strongly from baseline distortions and is thus not reproduced reliably. In addition, for modulation amplitudes comparable to or larger than the linewidth, contributions of higher-order sidebands are no longer negligible (modulation

* Corresponding authors. Fax: +41 1 632 1021 (A. Schweiger).
E-mail addresses: fedin@esr.phys.chem.ethz.ch (M. Fedin), schweiger@phys.chem.ethz.ch (A. Schweiger).
[1] On leave from Laboratory of Magnetic and Spin Phenomena, International Tomography Center, Novosibirsk 630090, Russia.
[2] On leave from MRS Laboratory, Kazan State University, Kazan 420008, Russia.

1090-7807/$ - see front matter © 2004 Elsevier Inc. All rights reserved.
doi:10.1016/j.jmr.2004.07.021

broadening), and thus integration of the first-harmonic spectrum will not result in the correct absorption spectrum. Some methods allow to take account of modulation broadening in simulations [3] or to correct for the modulation distortions by proper signal processing [4].

Several approaches have been proposed to measure absorption EPR spectra in CW mode. A scheme that can easily be implemented is mw source modulation [1]. In this technique, not only the EPR signal but also any unwanted reflections from the cavity will be modulated, so that their contribution is still present after demodulation. Therefore, the signal-to-noise ratio cannot be significantly improved using source modulation. Another approach makes use of multiple-photon EPR transitions, where three circularly polarized σ photons are simultaneously absorbed from two transverse mw fields with different frequencies [5]. However, this method is technically quite demanding, as it requires two mw sources and a stable locking of the phase between them. A technique based on large-amplitude square-wave field modulation applies only for narrow EPR lines [6].

Pulse EPR techniques are most often used to measure absorption line spectra. In echo-detected EPR, the amplitude of the electron spin echo is recorded as a function of the magnetic field, whereas in FID-detected EPR the integral over the free induction decay (FID) after an mw pulse is measured [7]. The major disadvantage of pulse approaches is that for most of the samples a detectable signal can only be obtained at low temperatures, where the relaxation times become sufficiently long. In addition, the lines of an echo-detected EPR spectrum are often distorted by field-dependent nuclear modulations [8,9]. FID detection is free from these distortions, but on the other hand, it requires the use of long and weak mw pulses, which leads to some loss in sensitivity. CW and pulse longitudinally detected EPR techniques are other alternatives to record an absorption spectrum, however, their sensitivity is usually quite low [10–12]. Inversion-recovery detected EPR combines pulse excitation and CW detection [13]. Since the cavity coupling cannot be optimized simultaneously for both excitation and detection, some trade-off has to be made.

In this paper, we describe a new type of a modulation experiment, which allows for the measurements of absorption line shapes in CW mode. The method can be carried out using a slightly modified CW-EPR setup. For spectra with broad lines the approach is superior to standard CW-EPR.

2. Theory

2.1. Basic idea

Consider the experiment shown in Fig. 1. In contrast to conventional CW-EPR, an amplitude modulation

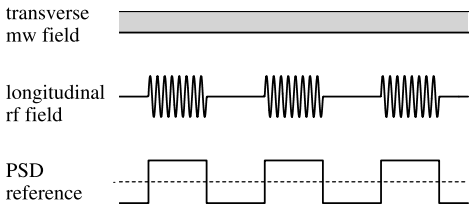

Fig. 1. Scheme for the AM-CW-EPR experiment. The transverse microwave field is continuously applied. The amplitude-modulated longitudinal rf field is described by $A_{\mathrm{am}}(t)\cos(\omega_{\mathrm{rf}}t + \varphi_{\mathrm{rf}})$, with radio frequency ω_{rf}, and the amplitude modulation function $A_{\mathrm{am}}(t)$ (step function with period $T = 2\pi/\omega_{\mathrm{am}}$). Phase-sensitive detection is done at frequency ω_{am}.

(AM) of the rf field with frequency ω_{am} is used, and detection with a phase-sensitive detector (PSD) is carried out with reference frequency $\omega_{\mathrm{ref}} = \omega_{\mathrm{am}}$. We describe now the basics of this AM-CW-EPR experiment and explain why slight saturation of the spin system is required to obtain absorption line EPR spectra.

When an $S = 1/2$ spin system is exposed to a bichromatic radiation field consisting of a transverse mw and a longitudinal rf field, multiple-photon transitions of the type $\sigma_{\mathrm{mw}} + k \times \pi_{\mathrm{rf}}$ are induced [2,14–16], where one circularly polarized σ_{mw} photon is absorbed from the transverse mw field, and k linearly polarized π_{rf} photons are absorbed (positive k) or emitted (negative k) from the longitudinal rf field. The frequencies of the transitions $\sigma_{\mathrm{mw}} + k \times \pi_{\mathrm{rf}}$ are $\omega_{\mathrm{mw}} + k\omega_{\mathrm{rf}}$, where ω_{mw} and ω_{rf} refer to the mw and radio frequencies.

The spin Hamiltonian in the laboratory frame can then be written as

$$\mathscr{H} = \omega_{\mathrm{S}} S_z + 2\omega_1 \cos(\omega_{\mathrm{mw}} t + \varphi_{\mathrm{mw}}) S_x + 2\omega_2 \cos(\omega_{\mathrm{rf}} t + \varphi_{\mathrm{rf}}) S_z, \quad (1)$$

where $2\omega_1$ and $2\omega_2$ are the amplitudes of the mw and rf field, φ_{mw} and φ_{rf} are the corresponding phases, $\omega_{\mathrm{S}} = -\gamma_{\mathrm{e}} B_0 = g\beta_{\mathrm{e}} B_0/\hbar$ is the electron Larmor frequency, and S_x, S_z, γ_{e}, g, β_{e}, and $\hbar$ have their usual meanings. For brevity, we consider in the following only the case $\varphi_{\mathrm{mw}} = \varphi_{\mathrm{rf}} = 0$.

By introducing an amplitude modulation of the longitudinal rf field, the Hamiltonian takes the form

$$\mathscr{H}_{\mathrm{am}} = \omega_{\mathrm{S}} S_z + 2\omega_1 \cos(\omega_{\mathrm{mw}} t) S_x + 2\omega_2 A_{\mathrm{am}}(t) \times \cos(\omega_{\mathrm{rf}} t) S_z, \quad (2)$$

where $A_{\mathrm{am}}(t)$ represents a rectangular function 1/0 with period $T = 2\pi/\omega_{\mathrm{am}}$ (see Fig. 1).

This amplitude modulation affects the observed signal in two ways. First, the amplitude of the transition at ω_{mw} (center band) is altered with ω_{am} due to the π-photon-induced transparency phenomenon [15]. π-photon-induced transparency is caused by destructive interference of many multiple-photon processes, which may reduce the amplitude of the single-photon transition up to zero, depending on the parameter

$z = 2\omega_2/\omega_{rf}$. Second, the amplitudes of the $\omega_{mw} + k \times \omega_{rf}$ transitions (sidebands) also depend on z. Both contributions cause a modulation of the observed signal with frequency ω_{am}.

2.2. Analytical description

For an analytical description of the experiment, the classical approach based on the modified Bloch equations is used, where the modulation of the magnetic field is taken into account [17]. It is convenient to introduce the new variable $m_{lab} = M_x + iM_y$, where M_x and M_y represent the x- and y-components of the magnetization vector in the laboratory frame, and to transform the coordinate system into a frame rotating with mw frequency ω_{mw} , i.e., $m = m_{lab}\exp(i\omega_{mw}t)$. The Bloch equations then have the form [17]

$$\begin{cases} \frac{dm}{dt} + i(\Omega_s + 2\omega_2 A_{am}(t)\cos(\omega_{rf}t))m + \frac{m}{T_2} - i\omega_1 M_z = 0 & \text{(a)} \\ \frac{dM_z}{dt} + \frac{M_z}{T_1} + \omega_1 \mathrm{Im}(m) = \frac{M_0}{T_1} & \text{(b)} \end{cases} \quad (3)$$

where $\Omega_s = \omega_S - \omega_{mw}$ is the resonance offset from the mw frequency, T_1 and T_2 are the longitudinal and transverse relaxation times, M_0 is the equilibrium magnetization, and M_z is the z-component of the magnetization vector. For $\omega_1 T_1 \ll 1$, saturation is negligible and Eq. (3b) simplifies to $M_z = M_0$ for $t \gg T_1$ [17]. Another simplification, which is relevant for our experiment, is to assume that $\omega_{am} \ll \omega_{rf}, 1/T_2$. This means, that a steady-state solution is reached between each step of the rectangular function $A_{am}(1 \to 0 \text{ or } 0 \to 1)$. We obtain then the solution [17]

$$m = i\omega_1 M_0 T_2 \sum_{n=-\infty}^{\infty} \sum_{k=-\infty}^{\infty} J_n(A_{am}(t)z) J_k(A_{am}(t)z) \times \frac{e^{i(n-k)\omega_{rf}t}(1 - iT_2(\Omega_s + n\omega_{rf}))}{1 + T_2^2(\Omega_s + n\omega_{rf})^2}, \quad (4)$$

with $z \equiv 2\omega_2/\omega_{rf}$ and the Bessel functions J_n and J_k of the first kind and nth and kth order [2,15,16]. For the absorptive part $\mathrm{Im}(m)$ of the DC component $(n - k = 0)$ we find

$$m_{DC} = \omega_1 M_0 T_2 \sum_{n=-\infty}^{\infty} J_n^2(A_{am}(t)z) \frac{1}{1 + T_2^2(\Omega_s + n\omega_{rf})^2}. \quad (5)$$

Assuming the reference of the PSD is a step function $1/-1$ with frequency ω_{am} (Fig. 1), the measured signal will be proportional to the difference $m_{DC}(z) - m_{DC}(0)$

$$P = \omega_1 M_0 T_2 \sum_{n=-\infty}^{\infty} [J_n^2(z) - J_n^2(0)] \frac{1}{1 + T_2^2(\Omega_s + n\omega_{rf})^2}. \quad (6)$$

Two examples for the line shapes obtained from Eq. (6) are shown in Fig. 2. The patterns in Fig. 2A consist of a number of lines separated by ω_{rf} and weighted with the

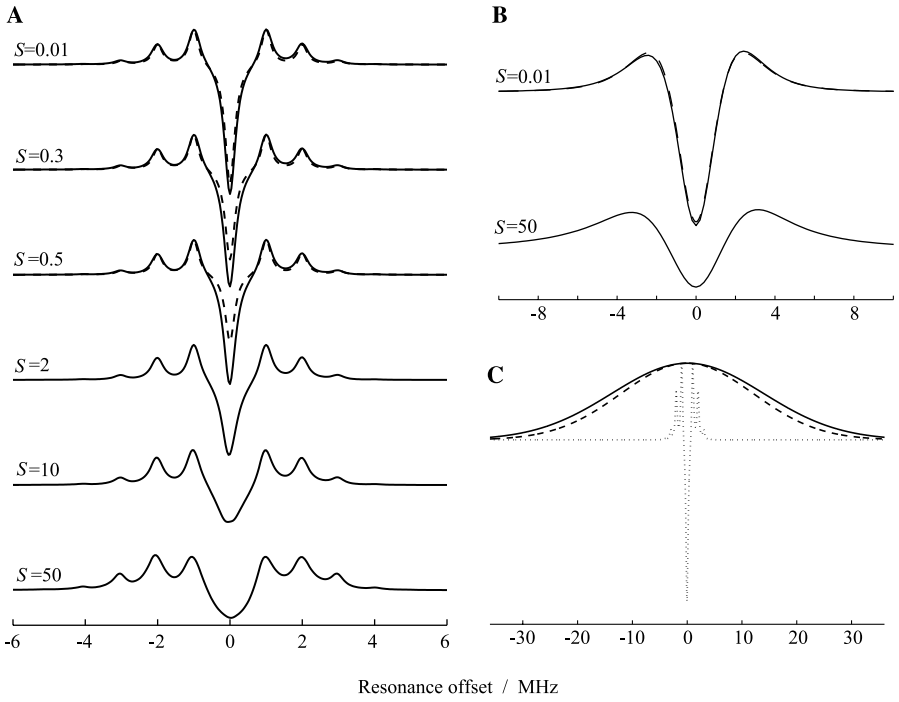

Fig. 2. (A) Analytical (dashed) and numerically simulated (solid) line patterns of AM-CW-EPR experiments for different values of the saturation parameter S (shown on the plot). All curves are normalized. Parameters: $T_1 = 100$ μs, $T_2 = 1$ μs, $\omega_{rf}/2\pi = 1$ MHz, $2\omega_2/\gamma_e = 0.08$ mT. (B) Analytical (dashed) and numerically simulated (solid) line patterns of AM-CW-EPR experiments for two values of the saturation parameter S (shown on the plot) when the individual sidebands are not resolved. All curves are normalized. Parameters: $T_1 = 100$ μs, $T_2 = 0.1$ μs, $\omega_{rf}/2\pi = 1$ MHz, $2\omega_2/\gamma_e = 0.08$ mT. (C) Line pattern for $S = 2$ from (A) (dotted), Gaussian line with width $\Delta_{FWHH} = 28.2$ MHz corresponding to ≈1 mT (dashed) and result of the convolution (solid). All curves are normalized.

Bessel function. The center band transition is always opposite in sign to the sideband transitions, since for any value of $z \neq 0$ one finds $J_0^2(z) - J_0^2(0) = J_0^2(z) - 1 < 0$ for the center band, and $J_{n\neq 0}^2(z) - J_{n\neq 0}^2(0) = J_{n\neq 0}^2(z) > 0$ for the sidebands. The amplitude of the center band transition decreases in the presence of modulation, while the amplitudes of the sidebands increase from zero to a certain value. The difference between these two situations (modulation on/off) then results in the patterns shown in Fig. 2.

The number of excited sidebands depends on z and the resolution of the individual lines on T_2. Fig. 2A shows the situation for $T_1 \gg T_2$, $1/T_2 < \omega_{rf}$ (slow relaxation), where the individual sidebands corresponding to the multiple-photon transitions $\sigma_{mw} + k \times \pi_{rf}$ are resolved. In Fig. 2B, the opposite case of spectra calculated for the situation $1/T_2 > \omega_{rf}$ (fast relaxation) is shown. The individual sidebands are then no longer resolved, and the line shape resembles a second-derivative absorption line.

The multi-line structures shown in Fig. 2A are unwanted features. To get true line shapes, one of the two situations has to be fulfilled: (1) ω_{rf} is much higher than the width of the entire spectrum, so that the first sideband is far away from the magnetic field region of interest, (2) ω_{rf} is much lower than the width of the entire spectrum. In addition, case (2) requires spectral lines that are *inhomogeneously* broadened.

The first case can only be achieved for very narrow EPR spectra, since it requires high radio frequencies and thus high rf amplitudes to provide sufficiently large values of $z = 2\omega_2/\omega_{rf}$. This kind of experiment was first described in [18]. For most samples with inhomogeneously broadened EPR lines, case (2) with low frequencies ω_{rf} is relevant, and only this situation will further be discussed. After averaging over the line inhomogeneity, the individual patterns in Figs. 2A and B will no longer be resolved.

An important requirement for the AM-CW-EPR experiment is that the integral I_P over the multi-line structure of each individual homogeneous line (center band and sidebands) is different from zero. However, from Eq. (6) it follows that:

$$I_P = \int_{-\infty}^{\infty} P \, d\Omega_s = 0, \tag{7}$$

since $\sum_{n=-\infty}^{\infty} J_n^2(z) \equiv 1$ for any value of z. Note, that the expressions in Eqs. (4)–(7) were obtained neglecting saturation. Since the individual multiple-photon transitions show a different saturation behavior [2], the integral will differ from zero when the spin system starts to be saturated.

An exact analytical solution of the modified Bloch equations including saturation is not straightforward, we therefore give only an approximate solution. The simplest way to include saturation with a small saturation parameter $S = \omega_1^2 T_1 T_2$ ($S \ll 1$), is to consider Eq. (4) as zero-order solution in an iterative process. By substituting Im(m) from Eq. (4) into Eq. (3b), a new value for M_z is obtained, which is used in Eq. (3a). Then, we again calculate the steady-state solution that is valid for $t \gg T_1$. To include saturation, it is sufficient to account only for the DC component of M_z

$$M_{z,sat} = M_0 \left(1 - S \sum_{n=-\infty}^{\infty} \frac{J_n^2(z)}{1 + T_2^2 (\Omega_s + n\omega_{rf})^2} \right). \tag{8}$$

Eq. (8) shows that saturation reduces the intensity of each individual multiple-photon transitions in a different way, and that the decrease is proportional to the saturation parameter S. By substituting Eq. (8) into Eq. (3a) we find for the absorptive DC component of m

$$m_{DC,sat} = \omega_1 T_2 M_0 \sum_{n=-\infty}^{\infty} \left(1 - S J_n^2(A_{am}(t)z)\right) J_n^2(A_{am}(t)z) \times \frac{1}{1 + T_2^2 (\Omega_s + n\omega_{rf})^2}. \tag{9}$$

Finally, using the definitions of $A_{am}(t)$ and the reference of the PSD we find

$$P_{sat} = \omega_1 T_2 M_0 \times \sum_{n=-\infty}^{\infty} \frac{\left[\left(1 - S J_n^2(z)\right) J_n^2(z) - \left(1 - S J_n^2(0)\right) J_n^2(0)\right]}{1 + T_2^2 (\Omega_s + n\omega_{rf})^2}. \tag{10}$$

The integral over the line pattern described by Eq. (10) is then given by

$$I_{P,sat} = \int_{-\infty}^{\infty} P_{sat} \, d\Omega_s = \omega_1 T_2 M_0 S \sum_{n=-\infty}^{\infty} \left[J_n^4(0) - J_n^4(z)\right] \int_{-\infty}^{\infty} \frac{d\Omega_s}{1 + T_2^2 (\Omega_s + n\omega_{rf})^2} = \pi \omega_1 M_0 S \sum_{n=-\infty}^{\infty} \left[J_n^4(0) - J_n^4(z)\right] = \pi \omega_1 M_0 S \left[1 - \sum_{n=-\infty}^{\infty} J_n^4(z)\right] > 0 \text{ for } z \neq 0 \tag{11}$$

From Eq. (11) we can conclude that the stronger the saturation, the larger is the integral. However, one should keep in mind that Eq. (11) is only valid for small values of S. For strong saturation, $I_{P,sat}$ should drop to zero with a maximum value for some intermediate saturation. Eq. (11) also shows that with increasing z the function $f(z) = 1 - \sum_{n=-\infty}^{\infty} J_n^4(z)$ rapidly approaches its maximum value $f_{max} = 1$ (e.g., f (5) = 0.88). This means that large signals do not require large rf amplitudes.

Fig. 2A (dashed lines) shows the influence of the saturation (for $S = 0.01, 0.3, 0.5$) on the line patterns created by the amplitude modulated longitudinal field. The center line experiences a stronger decrease than the sidebands, so that the integral becomes positive. Thus, for an inhomogeneously broadened line a pure absorption spectrum is obtained, which has negligible distortions if the width of the multi-line profile is much smaller than the width of the inhomogeneous line. This

is demonstrated in Fig. 2C, where the line pattern of Fig. 2A with $S = 2$ is convoluted with a Gaussian line of width $\Delta_{FWHH} \sim 1$ mT. The Gaussian line is slightly broadened by about the width of the multi-line pattern ($\sim 4\omega_{rf}$ in this case). However, for EPR lines with a width of several milli-Tesla and more, or for smaller values of ω_{rf} or $2\omega_2$, the difference becomes negligible and the original line shape is well reproduced.

2.3. Numerical simulations

The approximate analytical solution in Eq. (10), which is only valid for $S \ll 1$, was compared to exact numerical simulations, again based on the solution of the modified Bloch equations.

Fig. 2A demonstrates the good agreement between analytical and numerical results, as long as $S \ll 1$. For $S \approx 1$ the results obtained by the two approaches clearly deviate from each other, but the qualitative trend is still reproduced. For $S \gg 1$, the analytical expression in Eq. (10) does no longer apply and numerical simulations have to be used. They confirm that the center band experiences a stronger saturation than the sidebands, which is in agreement with the analytical results. The optimum condition (integral is maximum) is achieved, when the center band is significantly damped by saturation, but the sidebands are not. This condition is determined by an interplay of relaxation times, radio frequency, and rf and mw power.

3. Experimental

3.1. Instrumentation

The experiments were carried out on a commercial pulse X-band EPR spectrometer (Bruker Elexsys E580). The rf field parallel to the static magnetic field was produced by the rf coil of a pulse ENDOR probehead (Bruker ER 4118X-MD5-EN) rotated by 90° around its axis. The amplitude-modulated rf signal was generated by an arbitrary function generator (LeCroy LW420B) triggered by the spectrometer (modulation reference output) and amplified by a broadband amplifier (Amplifier Research, model 250A250A). Detection of the signal was done in a standard way using the built-in PSD operating at 100 kHz. Because of the large duty ratio for the rf field of 1/2 (50%), in all experiments we limited the maximum rf amplitude to 0.1–0.2 mT, to prevent rf coil damage.

The amplitude modulation was shaped by the step-function $A_{am}(t)$ (Fig. 1). It is important that the modulation signal fed to the rf coil does only contain the frequencies $\omega_{rf} \pm m\omega_{am}$, and not the frequency ω_{am}. A residual signal with frequency ω_{am} would cause a conventional CW-EPR signal, i.e., a derivative line on top of the pure absorption line would be observed. The DC components of the modulation signal have thus to be zero during both time intervals, $A_{am} = 1$ and $A_{am} = 0$ (ω_{rf} on/off). In all the experiments a high-pass filter was applied prior to rf amplification, and an integer number of periods of frequency ω_{rf} was used during $A_{am} = 1$.

AM-CW-EPR was also implemented on a commercial X-band CW-EPR spectrometer (Bruker Elexsys E500). The standard rectangular cavity TE_{101} was used. The amplitude-modulated signal was created and amplified as described above, and then delivered to the modulation coil of the cavity.

3.2. Samples

The spectrum of lithium phthalocyanine (LiPc), which was also used as a test sample in our previous work [2], consists of a single narrow line [19,20]. As a second test sample we used a coal sample provided by Bruker.

The powder sample of ^{63}Cu(II)-doped bis(salicylaldoximate)Ni(II) ($Ni(sal)_2$) had a Cu(II) concentration of about 1% [21]. The powder sample of Mn(II)imidazole ($Mn(II)(Im)_6$) diluted in $Zn(II)(Im)_6$ had a Mn(II) concentration of about 0.4% [22].

4. Results and discussion

In this section, we first demonstrate the basics of the new technique by using the two test samples LiPc and coal, and show two examples of AM-CW-EPR spectra of transition metal complexes with broad lines.

4.1. Experiments on test samples and comparison with theory

The EPR spectrum of LiPc recorded at room temperature consists of a single line which is mainly homogeneously broadened. Because of the small linewidth, it is the sample of choice to study the inner working of the AM-CW-EPR experiment.

The CW-EPR spectrum and a series of AM-CW-EPR spectra of LiPc are shown in Fig. 3A. The multi-line patterns clearly reproduce the shapes and trends predicted by the simulations shown in Fig. 2A. An increase in mw power results first in a linear increase in intensity of all the lines, until partial saturation is reached. At partial saturation conditions the center band is saturated more rapidly than the sidebands, in agreement with our theoretical findings (Fig. 2A). Fig. 3B shows two spectra obtained under conditions when the multi-line structure is not visible; the line shape of the spectra resembles the second derivative of an absorption line (Fig. 2B).

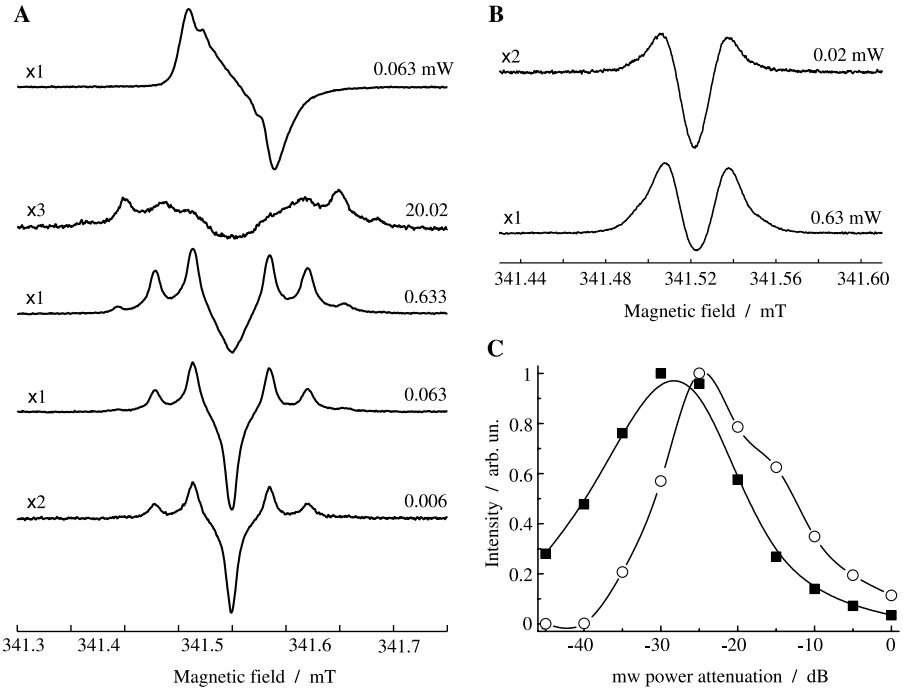

Fig. 3. (A) CW-EPR (top) and AM-CW-EPR (all others) spectra of LiPc recorded under different saturation conditions at room temperature. The mw power was varied, while all other parameters were kept constant. The values $\omega_{mod}/2\pi = 100$ kHz (modulation frequency), $2\omega_2/\gamma_e = 0.075$ mT were used in the CW-EPR spectrum (top). The values $\omega_{am}/2\pi = 100$ kHz, $\omega_{rf}/2\pi = 1$ MHz, and $2\omega_2/\gamma_e = 0.075$ mT were used in the AM–CW-EPR spectra. All plots are shown on the same scale, taking into account the scaling factors given on the left. The numbers on the right indicate the mw power. (B) AM-CW-EPR spectra of LiPc at room temperature when the individual sidebands are not resolved, with $\omega_{am}/2\pi = 100$ kHz, $\omega_{rf}/2\pi = 400$ kHz, and $2\omega_2/\gamma_e = 0.02$ mT. (C) Intensity of the CW-EPR lines (squares) and the integral over the AM-CW-EPR lines (circles) at different saturation conditions (different mw power). The two curves are normalized.

The integral over the multi-line pattern as a function of the mw power is shown in Fig. 3C and is compared to the corresponding CW-EPR line intensities. The maximum of the AM-CW-EPR intensity and its position are determined by an interplay between saturation of center band and sidebands. This means, that the maxima of the CW-EPR and the AM-CW-EPR intensity may be reached at different mw power (Fig. 3C). Thus, the observed spectra of LiPc and their dependence on mw power confirm our theoretical predictions and prove the requirement of partial saturation for AM-CW-EPR to become operative.

The spectrum of the coal sample consists of a single inhomogeneous line with a width of about 0.3 mT. The spectrum shown in Fig. 4A is obtained by using standard CW-EPR, while the spectra in Figs. 4B–D are obtained with AM-CW-EPR. Since the EPR line is inhomogeneously broadened, partial saturation is required to obtain the AM-CW-EPR spectra. The spectrum in Fig. 4B shows an absorption line shape, as predicted theoretically (Fig. 2C). The absolute intensity of this line is about two times higher than the intensity of the CW-EPR line recorded with the same mw power and the same modulation amplitude (for a discussion of AM-CW-EPR intensities, see Appendix). This confirms that AM-CW-EPR has superior sensitivity for broad

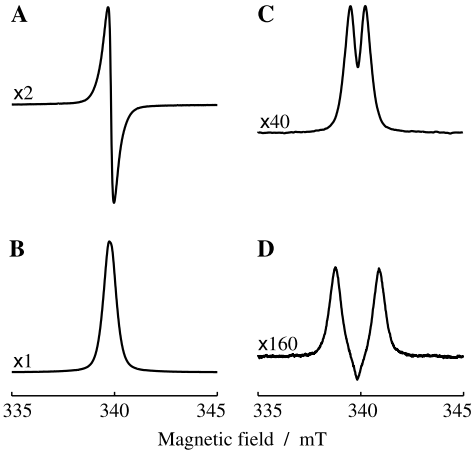

Fig. 4. Spectra of the coal sample recorded with CW-EPR and AM-CW-EPR at room temperature. The mw power (0.2 mW) and the modulation amplitude ($2\omega_2/\gamma_e = 0.025$ mT) were kept constant in all the experiments. (A) CW-EPR, $\omega_{mod}/2\pi = 100$ kHz. (B–D) AM-CW-EPR, $\omega_{am}/2\pi = 100$ kHz, and $\omega_{rf}/2\pi = 1$ MHz (B), 10 MHz (C), and 30 MHz (D). All the plots are shown on the same scale, taking into account the scaling factors shown on the left.

lines, and it is expected that the broader the line, the bigger the difference between CW-EPR and AM-CW-EPR sensitivity will be. When the modulation frequency becomes comparable with the linewidth, a splitting is

observed on top of the absorption spectrum (Fig. 4C). This splitting is of the order of $2\omega_{rf}$, and corresponds to the difference in the positions of the first low- and high-field sidebands. The higher-order sidebands are only weakly excited, since a value of $z = 2\omega_2/\omega_{rf} \approx 0.07$ was used. For even larger modulation frequencies the center band gets partially resolved (Fig. 4D), and the shape of the spectrum resembles those shown in Figs. 2B and 3B. Thus, to obtain an absorption line spectrum (Fig. 4B), one has to use frequencies and amplitudes of the rf field that are smaller than the width of the inhomogeneous line, similarly to CW-EPR.

In Fig. 5, the CW-EPR spectrum of the coal sample (A) is compared to the first derivatives of the AM-CW-EPR spectra (B–D) recorded with different values of ω_{rf}, but constant values of $z = 2\omega_2/\omega_{rf} \approx 0.7$. With the same modulation amplitude $2\omega_2$ and $\omega_{rf} = 400$ kHz, the line of the AM-CW-EPR spectrum (Fig. 5B) is only slightly broader ($\sim$0.085 mT) than the line of the CW-EPR spectrum (Fig. 5A). This additional broadening is determined by the width of the excited multi-line pattern (Fig. 2C), and corresponds in this experiment to about $6\omega_{rf}$, which means that sidebands up to $k = 3$ contribute to the spectrum. However, for lines of several milli-Tesla, this loss in spectral resolution is negligible, while the gain in sensitivity can be significant. For higher values of ω_{rf} (Figs. 5C and D) a further broadening is observed. The peculiarity in the center of the spectrum is caused by the splitting on top of the absorption spectrum, similar as found in Figs. 4C and D. Thus, smaller ω_{rf} values are preferable for better spectral resolution, as long as $\omega_{rf} < 2\omega_2$. Otherwise, the width of the multi-line profile will be determined by $2\omega_2$. On the other hand, there is also a lower limit for ω_{rf}, which is determined by several factors. First, an experiment at lower frequencies ω_{rf} requires lower frequency ω_{am} and thus longer time constants during phase sensitive detection. Second, the spacing ω_{rf}/γ_e between the lines corresponding to different multiple-photon transitions should exceed the amplitude of the mw field (i.e., $\omega_{rf} > 2\omega_1$). For $\omega_{rf} < 2\omega_1$, the center band and the sidebands up to index k, where $k\omega_{rf} \approx 2\omega_1$, will interfere. Hence, for high values of the mw power higher radio frequencies have to be used. We found that in our experiments radio frequencies between several hundreds of kHz and a few MHz, and rf field amplitudes up to 0.2 mT, provide a reasonable trade-off between spectral resolution and sensitivity.

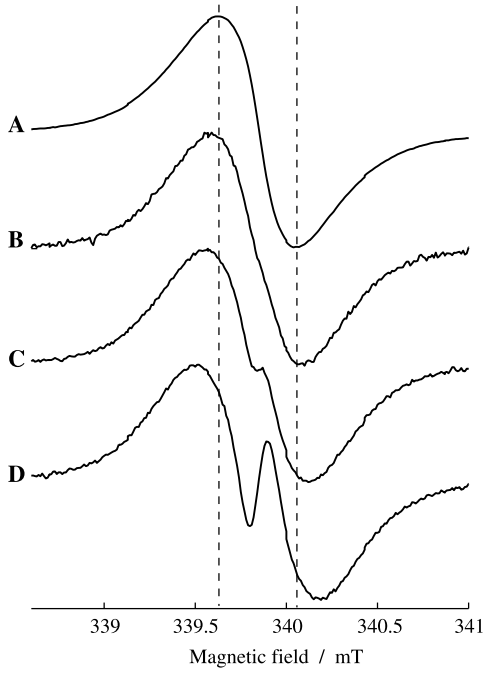

Fig. 5. Comparison of spectra of the coal sample recorded with CW-EPR and AM-CW-EPR at room temperature. (A) CW-EPR spectrum, $\omega_{mod}/2\pi = 100$ kHz, $2\omega_2/\gamma_e = 0.01$ mT. (B–D) first derivatives of the AM-CW-EPR spectra recorded with $\omega_{am}/2\pi = 100$ kHz and the same $z = 2\omega_2/\omega_{rf} \approx 0.7$ values. (B) $2\omega_2/\gamma_e = 0.01$ mT, $\omega_{rf}/2\pi = 400$ kHz, (C) $2\omega_2/\gamma_e = 0.025$ mT, $\omega_{rf}/2\pi = 1$ MHz, (D) $2\omega_2/\gamma_e = 0.05$ mT, and $\omega_{rf}/2\pi = 2$ MHz. The mw power was the same in all the experiments, and the intensities of all the spectra are normalized.

4.2. Application to broad-line spectra of transition metal complexes

In Fig. 6, the AM-CW-EPR spectrum of ^{63}Cu(II)-doped Ni(sal)$_2$ powder recorded at 100 K is compared with the corresponding CW-EPR and FID-detected EPR spectra. For the same modulation amplitude, the signal intensity of AM-CW-EPR significantly exceeds the one of CW-EPR (Figs. 6A and C). The CW-EPR spectrum (Fig. 6A) and the first derivative of the AM-CW-EPR spectrum (Fig. 6B) are very similar. This demonstrates the superiority of AM-CW-EPR for broad lines; there is virtually no loss in resolution, but the gain in sensitivity is significant.

The AM-CW-EPR spectrum (Fig. 6C) also agrees well with the FID-detected EPR spectrum recorded at 20 K (Fig. 6D). Although the sensitivity of the pulse technique can be higher than the one of AM-CW-EPR, the latter experiment has two advantages. The absorption spectrum can be measured with a CW-EPR spectrometer, and the temperature can be significantly higher in the AM-CW-EPR experiment. This is because the sensitivity of pulse techniques depends on the phase memory time, while for AM-CW-EPR, it depends on the longitudinal relaxation time as well, which is usually much longer.

Fig. 7 shows powder spectra of Mn(II)(Im)$_6$. The structure of the EPR spectra of Mn(II) complexes was studied in detail in [23]. The CW-EPR spectrum in Fig. 7A is dominated by six narrow lines. The AM-CW-EPR spectrum in Fig. 7C shows both broad and narrow lines simultaneously and is very close to the FID-detected EPR spectrum shown in Fig. 7D. The first

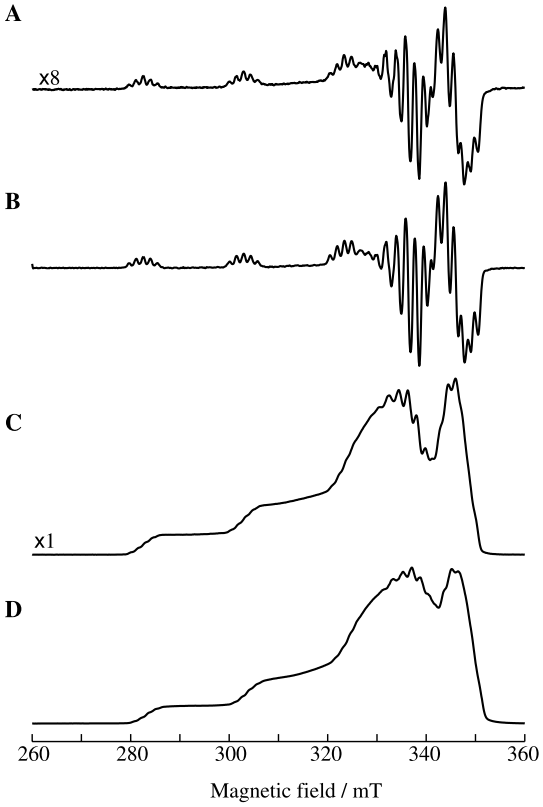

Fig. 6. Spectra of a ^{63}Cu(II)-doped Ni(sal)$_2$ powder sample recorded with CW-EPR, AM-CW-EPR, and pulse EPR. (A) CW-EPR, temperature 100 K, $\omega_{mod}/2\pi = 100$ kHz, $2\omega_2/\gamma_e = 0.025$ mT. (B) first derivative of the AM-CW-EPR spectrum (C). (C) AM-CW-EPR, temperature 100 K, $\omega_{am}/2\pi = 100$ kHz, $\omega_{rf}/2\pi = 1$ MHz, and $2\omega_2/\gamma_e = 0.025$ mT. (D) FID-detected EPR, temperature 20 K. The plots (A) and (C) are shown on the same scale, taking into account the scaling factors shown on the left, plots (B) and (D) are normalized for convenience.

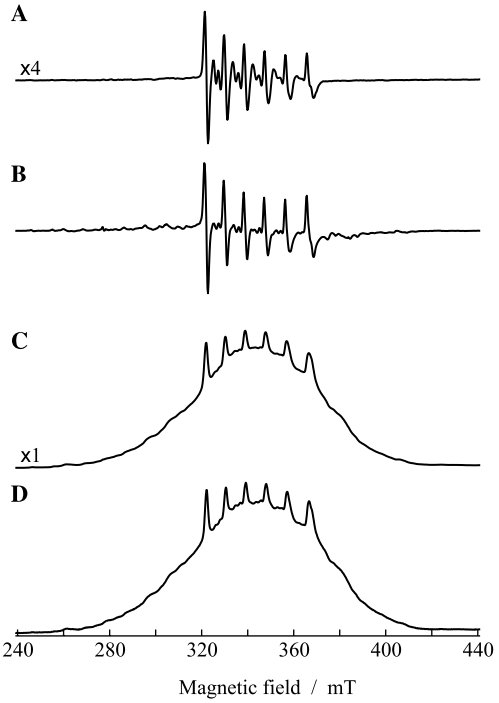

Fig. 7. Spectra of a Mn(II)(Im)$_6$ powder sample recorded with CW-EPR, AM-CW-EPR, and pulse EPR at 20 K. (A) CW-EPR, $\omega_{mod}/2\pi = 100$ kHz, $2\omega_2/\gamma_e = 0.025$ mT. (B) First derivative of the AM-CW-EPR spectrum (C). (C) AM-CW-EPR, $\omega_{am}/2\pi = 100$ kHz, $\omega_{rf}/2\pi = 400$ kHz, and $2\omega_2/\gamma_e = 0.025$ mT. (D) FID-detected EPR. The plots (A) and (C) are shown on the same scale, taking into account the scaling factors shown on the left, plots (B) and (D) are normalized for convenience. Sharp lines in the spectra originate from the EPR transitions $m_s = 1/2 \leftrightarrow -1/2$, $m_I = 5/2, 3/2, \ldots, -5/2$; broad lines are dominated by the EPR transitions $5/2 \leftrightarrow 3/2, 3/2 \leftrightarrow 1/2, -1/2 \leftrightarrow -3/2$, and $-3/2 \leftrightarrow -5/2$.

derivative of the AM-CW-EPR spectrum (Fig. 7B) is very similar to the CW-EPR spectrum, but in AM-CW-EPR contributions from the broad line are still observable, and the forbidden transitions (weak doublets between the six lines) are less pronounced. This reduction of the forbidden line intensities is caused by the fact that allowed transitions can more easily be saturated than forbidden ones. A similar effect has been observed in [5]. This suppression of the forbidden transitions in AM-CW-EPR spectrum is a further advantage, as this often leads to a simplification of the spectra.

In Mn(II)(Im)$_6$, the signal intensity of AM-CW-EPR is found to be considerably higher than the one of CW-EPR (Figs. 7A and C). It is remarkable, that the broad line is virtually indiscernible in the CW-EPR spectrum. It cannot reliably be obtained even using the maximum available modulation amplitude (3 mT), while in AM-CW-EPR a modulation amplitude as small as 0.025 mT already allows for the observation of this feature. The broad line can also not reliably be obtained by integrating the CW-EPR spectrum, as was discussed in the introduction. This clearly demonstrates the sensitivity improvement of AM-CW-EPR for broad EPR lines.

Note, that AM-CW-EPR can also be implemented on standard CW-EPR spectrometers. For example, the experiments shown in Figs. 6A–C were well reproduced at a commercial CW-EPR spectrometer. As additional equipment only an rf generator and an rf amplifier were required.

5. Outlook

The experiment introduced in this work allows for the measurement of absorption EPR spectra. Under optimum conditions, the method is more sensitive than conventional CW-EPR. The major requirements are partial saturation and an amplitude and frequency of the modulation field which are smaller than the desired spectral resolution. The technique is straightforward and does not require advanced equipment. It can be carried out by using a standard CW-EPR spectrometer with an only slightly modified configuration, or by using a pulse or CW-ENDOR setup. As one of the trends in EPR is to

go to higher mw frequencies where EPR spectra generally become broader, high-field AM-CW-EPR represents a useful alternative to standard high-field CW-EPR.

Acknowledgments

We thank Dr. Moritz Kälin for his stimulating contributions in the early stage of this work. We thank Dr. Ines Garcia-Rubio for providing us with the $Mn(II)(Im)_6$ sample and Jörg Forrer for technical assistance. This research has been supported by the Swiss National Science Foundation.

Appendix

For a comparison of CW-EPR and AM-CW-EPR sensitivities, the signal-to-noise ratios in corresponding spectra were analyzed. The conditions of phase-sensitive detection were identical, resulting in the same noise level for both experiments. Therefore, the intensities of the signals could directly be compared. In addition, the following aspects have to be considered:

(1) For CW-EPR the sensitivity increases with increasing modulation amplitude $2\omega_2$, as long as $2\omega_2$ is smaller than the linewidth, while for AM-CW-EPR the dependence on $2\omega_2$ is described by the function $f(z) = 1 - \sum_{n=-\infty}^{\infty} J_n^4(2\omega_2/\omega_{rf})$ [Eq. (11)], which approaches its maximum at low values of $2\omega_2$. Therefore, a comparison of the two techniques using the same values of $2\omega_2$ can in principle give different results depending on $2\omega_2$. A comparison can only be made using $2\omega_2/\gamma_e < 0.2$ mT, as higher rf fields cannot be produced with a duty ratio of 1/2 by the ENDOR coil of the commercial Bruker probhead. However, also in CW-EPR low values of $2\omega_2$ have to be used to avoid line broadening and baseline distortions. Thus, we make a comparison using the same low values of $2\omega_2$, and give additional comments in Section 4.2 about the sensitivity of CW-EPR for large values of $2\omega_2$.

(2) The optimum mw power can be different for CW-EPR and AM-CW-EPR, as is discussed in Section 4.1 (Fig. 3C). We therefore use the same values for the mw power $2\omega_1$, but for the saturation parameter we use $S < 1$, i.e., in a range where both the sensitivity of CW-EPR and AM-CW-EPR increases with increasing $2\omega_1$. Often it is even not possible to achieve $S > 1$ experimentally.

(3) There are two frequencies involved in AM-CW-EPR, ω_{rf} and ω_{am}, while CW-EPR uses only one modulation frequency ω_{mod}. The frequencies ω_{mod} and ω_{am} can be taken equal, while the second frequency ω_{rf} is a free parameter, which influences both the sensitivity and the spectral resolution. The required spectral resolution in turn depends on the linewidths. Thus, in all the experiments phase-sensitive detection was done at the same frequency $\omega_{mod} = \omega_{am}$. A frequency ω_{rf} as low as possible was chosen, which had to fulfill the condition $\omega_{rf} > 2\omega_1$, as discussed in the last paragraph of Section 4.1.

(4) The sensitivity of CW-EPR and AM-CW-EPR shows a different temperature dependence. For AM-CW-EPR to become operative it is necessary to reach at least slight saturation. Therefore, in the experiments in Section 4.2 the temperature was lowered. At room temperature the sensitivity of CW-EPR was significantly higher than for AM-CW-EPR, as saturation of both samples was negligible. At low temperatures the situation was reversed.

Thus, it is difficult to compare CW-EPR and AM-CW-EPR sensitivities. However, the sensitivity of AM-CW-EPR can significantly exceed the one of CW-EPR, so that the former approach is superior for any values of mw power and modulation amplitude available in our experiments (Section 4.2).

References

[1] C.P. Poole, Electron Spin Resonance: A Comprehensive Treatise of Experimental Techniques, Wiley, New York, 1983.
[2] M. Kälin, I. Gromov, A. Schweiger, The continuous wave electron paramagnetic resonance experiment revisited, J. Magn. Reson. 160 (2003) 166.
[3] B.H. Robinson, C. Mailer, A.W. Reese, Linewidth analysis of spin labels in liquids, J. Magn. Reson. 138 (1999) 199.
[4] V.A. Bikineev, E.A. Zavatskii, V.V. Isaevivanov, V.V. Lavrov, A.V. Lomakin, V.N. Fomichev, K.A. Shabalin, Methods for the correction of modulation distortions of line-shapes in the spectroscopy of electron-paramagnetic-resonance, Zh. Tekh. Fiz. 65 (1995) 177.
[5] H.S. Mchaourab, S. Pfenninger, W.E. Antholine, C.C. Felix, J.S. Hyde, P.H. Kroneck, Multiquantum EPR of the mixed-valence copper site in nitrous-oxide reductase, Biophys. J. 64 (1993) 1576.
[6] M. Bonori, C. Franconi, P. Galuppi, M. Guerrisi, A field modulation-detection scheme for high-sensitivity, quantitative magnetic-resonance spectroscopy, Meas. Sci. Technol. 2 (1991) 1046.
[7] A. Schweiger, G. Jeschke, Principles of Pulse Electron Paramagnetic Resonance, Oxford University Press, London, 2001.
[8] W.B. Mims, J.L. Davis, Proton modulation of the electron spin echo envelope in a Nd^{3+}: aquo glass, J. Chem. Phys. 64 (1976) 4836.
[9] D. Goldfarb, L. Kevan, Effect of nuclear modulation on field-swept electron spin-echo spectra, J. Magn. Reson. 76 (1988) 276.
[10] F. Chiarini, M. Martinelli, F.A. Rolla, S. Santucci, Periodic longitudinal magnetization of a spin system irradiated with two transverse radio-frequency waves, Phys. Lett. A 44 (1973) 91.
[11] M. Martinelli, L. Pardi, C. Pinzino, S. Santucci, Dependence on relaxation times of longitudinally detected paramagnetic resonance, Solid State Commun. 17 (1975) 211.

[12] A. Schweiger, R.R. Ernst, Pulsed electron-spin-resonance with longitudinal detection—a novel recording technique, J. Magn. Reson. 77 (1988) 512.
[13] E. Hoffmann, A. Schweiger, Inversion-recovery detected EPR, Appl. Magn. Reson. 9 (1995) 1.
[14] I. Gromov, A. Schweiger, Multiphoton resonances in pulse EPR, J. Magn. Reson. 146 (2000) 110.
[15] M. Kälin, I. Gromov, A. Schweiger, Transparency in two-level spin systems induced by a longitudinal field, Phys. Rev. A 69 (2004) 033809.
[16] M. Fedin, M. Kälin, I. Gromov, A. Schweiger, Applications of π-photon-induced transparency in two-frequency pulse electron paramagnetic resonance experiments, J. Chem. Phys. 120 (2004) 1361.
[17] O. Haworth, R.E. Richards, The use of modulation in magnetic resonance, in: J.W. Emsley, J. Feeney, L.H. Sutcliffe (Eds.), Progress in Nuclear Magnetic Resonance Spectroscopy, vol. 1, Pergamon, New York, 1966, p. 1.
[18] M. Kälin, Multiple photon processes in EPR spectroscopy, PhD. thesis No.15142, ETH Zürich, 2003. Available from: <http://e-collection.ethbib.ethz.ch/show?type=diss&nr=15142;> copies are available on request from the corresponding author.
[19] G. Ilangovan, J.L. Zweier, P. Kuppusamy, Electrochemical preparation and EPR studies of lithium phthalocyanine. Part 2: Particle-size-dependent line broadening by molecular oxygen and its implications as an oximetry probe, J. Phys. Chem. B 104 (2000) 9404.
[20] P. Turek, J.-J. Andre, J. Simon, Radicalar semiconductors. 3. Extreme spin exchange narrowing in a neutral phthalocyanine radical—the lithium phthalocyanine, Solid State Commun. 63 (1987) 741.
[21] E.G. Cox, F.W. Pinkard, W. Wardlaw, K.C. Webster, Planar configuration for guadricovalent nickel, palladium and platinum, J. Chem. Soc. (1935) 459.
[22] C. Sandmark, C.-I. Bränden, The crystal structure of hexaimidazole zink(II) dichloride tetrahydrate, $Zn(C_3H_4N_2)_6Cl_2{\cdot}4H_2O$, Acta Chem. Scand. 21 (1967) 993.
[23] B.E. Sturgeon, J.A. Ball, D.W. Randall, R.D. Britt, ^{55}Mn electron spin echo ENDOR of Mn^{2+} complexes, J. Phys. Chem. 98 (1994) 12871.